





Annual integral solar proton fluences for 1984–2019[★]

O. Raukunen^{1,2} , I. Usoskin³ , S. Koldobskiy³ , G. Kovaltsov³, and R. Vainio¹ 

¹ Space Research Laboratory, University of Turku, Turku, Finland
e-mail: oajrau@utu.fi

² Aboa Space Research Oy, Turku, Finland

³ Space Physics and Astronomy Research Unit and Sodankylä Geophysical Observatory, University of Oulu, Oulu, Finland

Received 8 April 2022 / Accepted 17 June 2022

ABSTRACT

Aims. Long-term fluxes or integral fluences of solar energetic particles (SEPs), and their variability within and beyond the 11-year solar cycle, make an important contribution to space physics. However, large uncertainties exist in the evaluation of average SEP fluxes or fluences over the last few decades, as they have been assessed by different methods and from different datasets. Here we revisit the derivation of annual integral SEP fluences from available data based on in situ measurements since 1984.

Methods. We reconstructed a full time series of integral SEP fluxes above 10, 30, 60, 100, and 200 MeV for the period from 1984 to 2019 using observations performed by the GOES satellites. Intercalibration of the fluxes was performed via a linear relation between overlapping pairs of observations in order to obtain a uniform dataset. Galactic cosmic ray (GCR) background subtraction and identification of SEP event periods were carefully performed, allowing for a precise calculation of annual SEP fluences.

Results. Annual integral fluences of SEPs with energies above 10, 30, 60, 100, and 200 MeV were calculated for the period from 1984 to 2019 (solar cycles 22–24), along with their uncertainties. It is shown that solar cycle 24 was significantly (by a factor of 5–8) weaker in the SEP fluence than the preceding cycles 22 and 23. The cumulative occurrence probability of years with the fluence above a given value is found to be perfectly described by the Weibull distribution. This can be used as a projection for the occurrence of solar extreme eruptive events on the secular timescales.

Key words. Sun: particle emission – Sun: flares – Sun: activity – solar-terrestrial relations

1. Introduction

There are two main components of the near-Earth interplanetary radiation environment: an always-present, slowly varying flux of energetic galactic cosmic rays (GCRs), and a highly variable flux of less energetic solar energetic particles (SEPs). While GCRs dominate in the energy range above several hundred MeV, the lower-energy range is defined by SEPs. The averaged flux of SEPs is formed by sporadic SEP events when the SEP intensity can exceed the background level by many orders of magnitude. On one hand, studies and analyses of SEP events form an important branch of solar physics, providing information on, for example, solar eruptive processes, particle acceleration, and transport in heliospheric plasma (e.g. Vainio et al. 2009; Desai & Giacalone 2016). On the other hand, the averaged fluxes of lower-energy particles, where SEPs dominate, are important for information on, for example, long-term solar-terrestrial relationships, near-Earth radiation environment, atmospheric chemistry, and cosmogenic isotopes.

Traditionally, SEP fluences are provided as integrated fluxes of energetic particles (protons) with energy above a given threshold E_0 , denoted henceforth as $F_{E_0} \equiv F(>E_0)$. Usually, several typical E_0 energies are considered: 10 MeV, 30 MeV, 60 MeV, and sometimes 100 MeV, the corresponding integral fluences being F_{10} – F_{100} as important for space weather and terrestrial applications (e.g. Feynman & Gabriel 2000; Reames 2013;

Klein & Dalla 2017). Additionally, it has been shown recently that the F_{200} SEP fluence is representative of ground-based detections of SEP events (ground level enhancements, GLEs) by neutron monitors (Kovaltsov et al. 2014) and of the production of cosmogenic isotopes (Koldobskiy et al. 2022). Independently of direct measurements, average fluxes of SEPs in the energy range between 30 and 80 MeV can be estimated over timescales of thousands and millions of years using measurements of cosmogenic isotopes in lunar rocks (e.g. Reedy 2012; Poluianov et al. 2018).

The average SEP fluxes are usually represented via annual fluences (flux integrated over the calendar year) or over a solar cycle. Several efforts in systematization of the fluxes and fluences of SEPs were performed in the past. Many studies focused on the top strongest SEP events: for example, King (1974) assessed the F_{10} , F_{30} , F_{60} , and F_{100} fluences for the period 1966–1972; Goswami et al. (1988) estimated F_{10} , F_{30} , F_{60} , and F_{92} for major SEP events for the period 1972–1986; Shea & Smart (1990) provided the solar-cycle averaged values of F_{10} and F_{30} for cycles 19–21; Feynman et al. (1990) evaluated the F_{10} and F_{30} top fluences for cycles 19–21; Shea & Smart (1992) and Smart & Shea (2002) provided averaged F_{10} and F_{30} fluences for cycles 19–22; Feynman et al. (1993) estimated the F_{10} , F_{30} , and F_{60} fluences for the top ten SEP events for 1963–1991; Reedy (1998) provided estimates of F_{10} , F_{30} , F_{60} , and F_{100} averaged over solar cycles 19–22; Jun et al. (2007) defined the F_{11} , F_{27} , F_{61} , and F_{95} fluences for 135 major events for 1973–1997; Reedy (2012) (updated as Reedy 2014) assessed cycle-averaged fluences F_{10} , F_{30} , and F_{60} for solar cycles 19–24; Tylka et al. (2005) analysed several fluence values for 44 SEP events for 1997–2003;

[★] The annual fluences and hourly integral fluxes are available in electronic form at the CDS via anonymous ftp to cdsarc.u-strasbg.fr (130.79.128.5) or via <http://cdsarc.u-strasbg.fr/viz-bin/cat/J/A+A/665/A65>

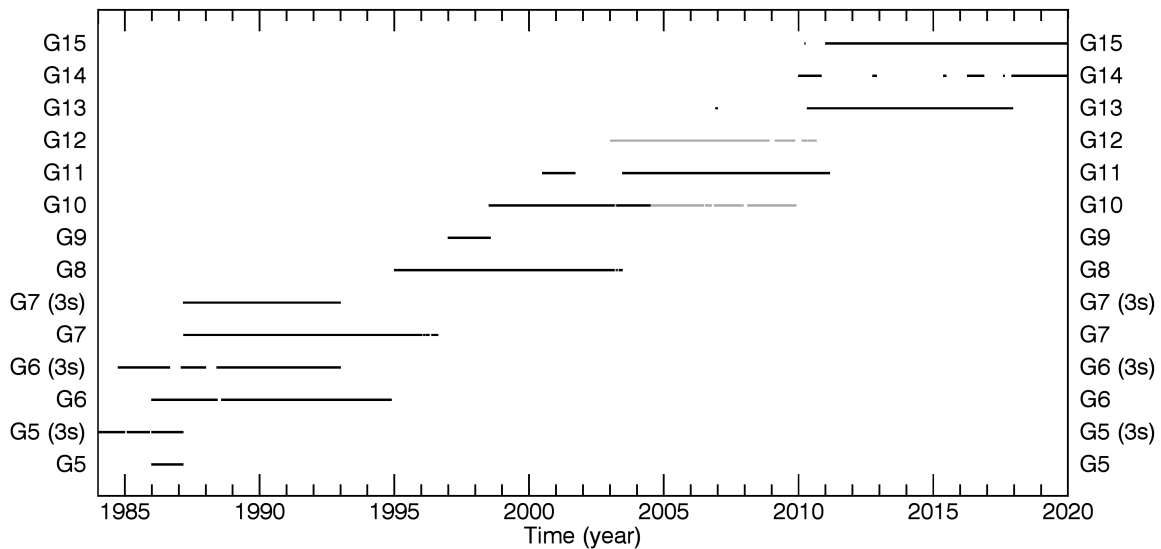


Fig. 1. Availability of proton data from GOES-5 to GOES-15. The grey lines show times when measurements from the high-energy channels P6 and P7 were not available.

Tylka & Dietrich (2009) and Raukunen et al. (2018) analysed major GLE events and reconstructed their spectra for solar cycles 19–24, and the study was methodologically updated by Koldobskiy et al. (2021); Bazilevskaya et al. (2014) provided F_{10} for the largest SEP events of cycles 19–24; Jiggins et al. (2014) evaluated F_{10} , F_{30} , F_{60} , and F_{100} fluences for the strongest SEP events in August 1972 and October 1989; and Cohen & Mewaldt (2018) analysed the top ten SEP events of cycles 23 and 24.

Most of those studies focused on analyses of spacecraft data for major SEP events so that the annual or cycle-average fluences were obtained by summing them up. There are, however, uncertainties related to the definition of the event selection, duration (sometimes limited to 24 h), and background levels. In addition, systematic biases were known in some spacecraft-borne particle detectors that may have distorted the estimated fluences. Because of the long duration and relative consistency of the energetic particle observations performed by the Geostationary Operational Environmental Satellites (GOES) operated by the National Oceanic and Atmospheric Administration (NOAA), it has been utilized by several studies on SEP fluxes and fluences at timescales longer than a solar cycle (e.g. Xapsos et al. 2000, 2006; Rosenqvist et al. 2005; Firoz et al. 2010; Atwell et al. 2015; Mewaldt et al. 2015; Papaioannou et al. 2016; Robinson et al. 2018). Many studies have been performed to improve the uniformity of the multi-satellite measurement series via intercalibration, cross-calibration, or bow-tie analysis¹ of response functions (e.g. Jiggins et al. 2012, 2018; Sandberg et al. 2014; Rodriguez et al. 2014, 2017; Bruno 2017; Raukunen et al. 2020; Hu & Semones 2022).

In this work, we perform a new reconstruction of the annual fluences F_{10} , F_{30} , F_{60} , F_{100} , and F_{200} for the period 1984–2019 using direct spacecraft data and applying updated methodology both in the approach (we do not separate individual SEP events but compute the annual fluences directly) and in the data

analysis (improved bias correction and intercalibration procedures are used).

2. Data

2.1. Selection and processing

We used the five-minute averaged proton fluxes² observed by the Energetic Particle Sensor (EPS; Onsager et al. 1996; Hanser 2011) on board the GOES satellites. All GOES satellites from GOES-1–12 included an EPS unit as part of their Space Environment Monitor (SEM) subsystem, and the SEM onboard GOES-13–15 included two units, also known as Energetic Proton, Electron, and Alpha Detectors (EPEADs). The design of EPS/EPEAD includes a telescope and three dome detectors, providing seven proton channels, P1–P7, with energies ranging from 0.6 MeV to 500 MeV. Since the P1 channel mostly measures low-energy trapped protons and the topic of this study is medium and high-energy SEPs, we didn’t use those data in our analyses. Apart from a decrease in the geometric factor of one dome detector from GOES-8 onwards, the design of the EPS has remained unchanged from GOES-4 to GOES-15 (e.g. Rodriguez et al. 2014). Starting from GOES-16, launched in November 2016, the energetic proton observations are performed by a completely new instrument, the Solar and Galactic Proton Sensor (SGPS; Kress et al. 2020). Data from the final EPS onboard GOES-15 were discontinued in March 2020, and while the overlap allows for cross-calibration of the EPS and the SGPS (Kress et al. 2021), we restrict our study to only EPS observations until the end of 2019, that is, the end of solar cycle 24.

The availability of data from satellites GOES-5 through GOES-15 is shown in Fig. 1 with a black line. The grey line (in the cases of GOES-10 and GOES-12) shows times when measurements from the highest-energy channels P6 and P7 were not available, which makes these data unusable in this study by preventing the calculation of integral fluxes. In the cases of GOES-5, GOES-6, and GOES-7, two datasets were available: the ‘original’ dataset, and a recently revised dataset, denoted with suffix ‘3s’. In addition to the ‘raw’ differential proton fluxes,

¹ Bow-tie analysis, originally described by Van Allen et al. (1974), is a method of estimating the effective energy and geometric factor of an instrument channel by taking into account the calibrated response function and the spectra that the instrument is assumed to observe. Folding the response function with a range of spectra results in a bow-tie shaped family of curves for the geometric factor as a function of effective energy, and the optimal values are found at the knot of the bow-tie.

² CSV files downloaded from <https://satdat.ngdc.noaa.gov/sem/goes/data/avg/> on 2021-07-21.

the original data files provide differential proton fluxes corrected for GCR background and high-energy contamination, as well as integral proton fluxes above 1, 5, 10, 30, 50, 60, and 100 MeV, denoted henceforth as f_1 , f_5 , f_{10} , f_{30} , f_{50} , f_{60} , and f_{100} (see the appendix of [Rodríguez et al. 2017](#), for a description of the Z89 algorithm used in the data processing). Since neither the corrected nor the integral fluxes are provided in the 3s data, we chose to base our study on the raw, or uncorrected, fluxes. In the cases of GOES-13–15, we used the orientation flag data files³ to select fluxes observed by the westward-facing EPEAD.

The proton fluxes, especially those observed by the first generation of satellites (GOES-5 to GOES-7 in our study), contain dropouts, spikes, and periods of suspicious values of between a few hours and a few days. It should be noted, however, that the 3s datasets seemed to suffer much less from these problems than the corresponding original datasets. To remove the dropouts, we scanned through each channel of each detector and removed datapoints f_i , which fulfilled the criterion $f_i < 0.1 \cdot \text{med}(f_{i-6}, \dots, f_{i+6})$, in other words, all values lower than 0.1 times the median of the surrounding 13 datapoints (including the point itself). Similarly, we removed the spikes with criteria $f_i > 10 \cdot \text{med}(f_{i-6}, \dots, f_{i+6})$ for channels P1–P4 and $f_i > 4 \cdot \text{med}(f_{i-6}, \dots, f_{i+6})$ for channels P5–P7. In order not to affect quiet time background, we added a condition for channels P2 and P3 that points with fewer than ten counts were not removed (see Appendix A for details on how the counts were defined). The periods of suspicious data were identified and removed manually from the time series. All of these periods occurred during times with no detectable SEP activity. In addition, a few erroneously high flux spikes during SEP activity, not caught by the spike criterion, were removed from GOES-6 channels P5–P7 between 20 December 1990 and 25 December 1990, and from GOES-10 channel P7 on 29 May 2001.

After cleaning all the individual datasets, we performed a comparison between each two overlapping differential datasets. As expected, there was almost 100% agreement between the original and the 3s datasets when the problematic datapoints were removed. In general, there was a decent agreement between the fluxes observed by the first generation (GOES-5 to GOES-7), as well as between the later generations (GOES-8 to GOES-15). However, there was a noticeable difference between the fluxes observed by GOES-7 and GOES-8 in channels P4–P7, which we assumed to be caused by the use of a different geometric factor in the data processing of the first GOES generation; see Appendix A for more details. Since there was no obvious disagreement between the later GOES generations, and the data are well studied (e.g. [Rodríguez et al. 2014, 2017](#)), we decided to correct the first generation data to better match the later generations by multiplying the fluxes with the GdE values derived in Appendix A and then dividing the resulting counting rates by the GdE values given in [Rodríguez et al. \(2014, 2017\)](#).

We quantified the agreement between the datasets by means of linear relationships between the measured fluxes f_x and f_y :

$$f_y = a + b f_x. \quad (1)$$

Similarly to [Rodríguez et al. \(2014\)](#), the parameters a and b were calculated with the least absolute deviation (LAD) method and their errors estimated with the bootstrap method (e.g. [Efron & Tibshirani 1986](#)). For each comparison, we used data from the full overlapping period, but to prevent the non-solar background affecting the fits too much, only points where a count threshold

(ten counts for P2–P3, 40 for P4–P5, and 100 for P6–P7) was exceeded in both instruments were included in the fit. In addition, to make sure that the fitting succeeded and the parameters made sense, we required there to be at least one point with ten times the count threshold in both compared instruments. If the requirement was not fulfilled, the fitting was performed without the intercept term, using all points. As an example, Fig. 2 shows the comparison between GOES-8 and GOES-11, along with the fits. The slopes and intercepts of the fits, along with their errors, for all overlapping observation pairs are listed in Tables B.1 and B.2. The majority of the differences between the observations are within 30%; however, channel P4 exhibits large variations in GOES-5–8, for which we did not find any apparent reason. Our results for GOES-8–15 agree quite well with the intercalibration results in [Rodríguez et al. \(2014\)](#), and any differences can most likely be explained by different selection of points.

2.2. Integral fluxes

In order to calculate the integral proton fluxes of solar origin, we subtracted the GCR background from the differential fluxes. The background flux is defined as the smallest daily flux for each ten-day period, calculated separately for each channel of each EPS/EPEAD instrument. In order to prevent long-duration SEP events or lingering data problems affecting the background, each background value greater than 1.5 times or smaller than 0.5 times the mean of three previous background values was replaced with the mean.

To improve the uniformity of the data, we selected GOES-8 as the baseline and corrected each differential channel of the other selected data sources to the same level using the intercalibration results given in Table B.1. GOES-8 was selected because of its coverage, as well as its data quality ([Rodríguez et al. 2017](#)). In cases where there was no overlap or it was too small, we used intermediate steps, namely: GOES-8 → GOES-7 → GOES-6 (3s) → GOES-5 (3s) and GOES-8 → GOES-11 → GOES-13 → GOES-15. However, it should be noted that the overlap between GOES-8 and GOES-7 covers only one, relatively small SEP event, which increases the total uncertainty of the results for GOES-5–7.

The integral fluxes were calculated using background-subtracted, one-hour averaged differential fluxes, assuming a piecewise power-law between the ‘effective’ channel energies E_{ch} , which were defined as

$$E_{\text{ch}} = \left(\frac{(-\gamma + 1)(E_h - E_l)}{E_h^{-\gamma+1} - E_l^{-\gamma+1}} \right)^{\frac{1}{\gamma}}, \quad (2)$$

where E_l and E_h are the channel’s lower and upper energy limits, respectively, and γ is the exponent of the power law spectrum ([Lafferty & Wyatt 1995](#); [Rodríguez et al. 2017](#)). Instead of the commonly used value $\gamma = 2$, which results in the geometric mean of the channel limits, we used $\gamma = 3$, which describes an SEP event spectrum more realistically above ~ 10 MeV energies (e.g. [Tylka & Lee 2006](#); [Mewaldt et al. 2012](#); [Raukunen et al. 2018](#)). The resulting effective energies are given in Table 1.

Because of the large discrepancies between channel P4 of GOES-5–8 (see Tables B.1 and B.2), we decided to omit this channel and to replace it by integrating between channels P3 and P5. In addition, we noticed a spectral discrepancy in channel P6 (see Appendix C for details), and decided to omit it as well. The integral flux above the highest differential channel P7 was calculated by subtracting 0.86 from the power law between channels

³ CSV files downloaded from <https://satdat.ngdc.noaa.gov/sem/goes/data/avg/> on 2021-07-21.

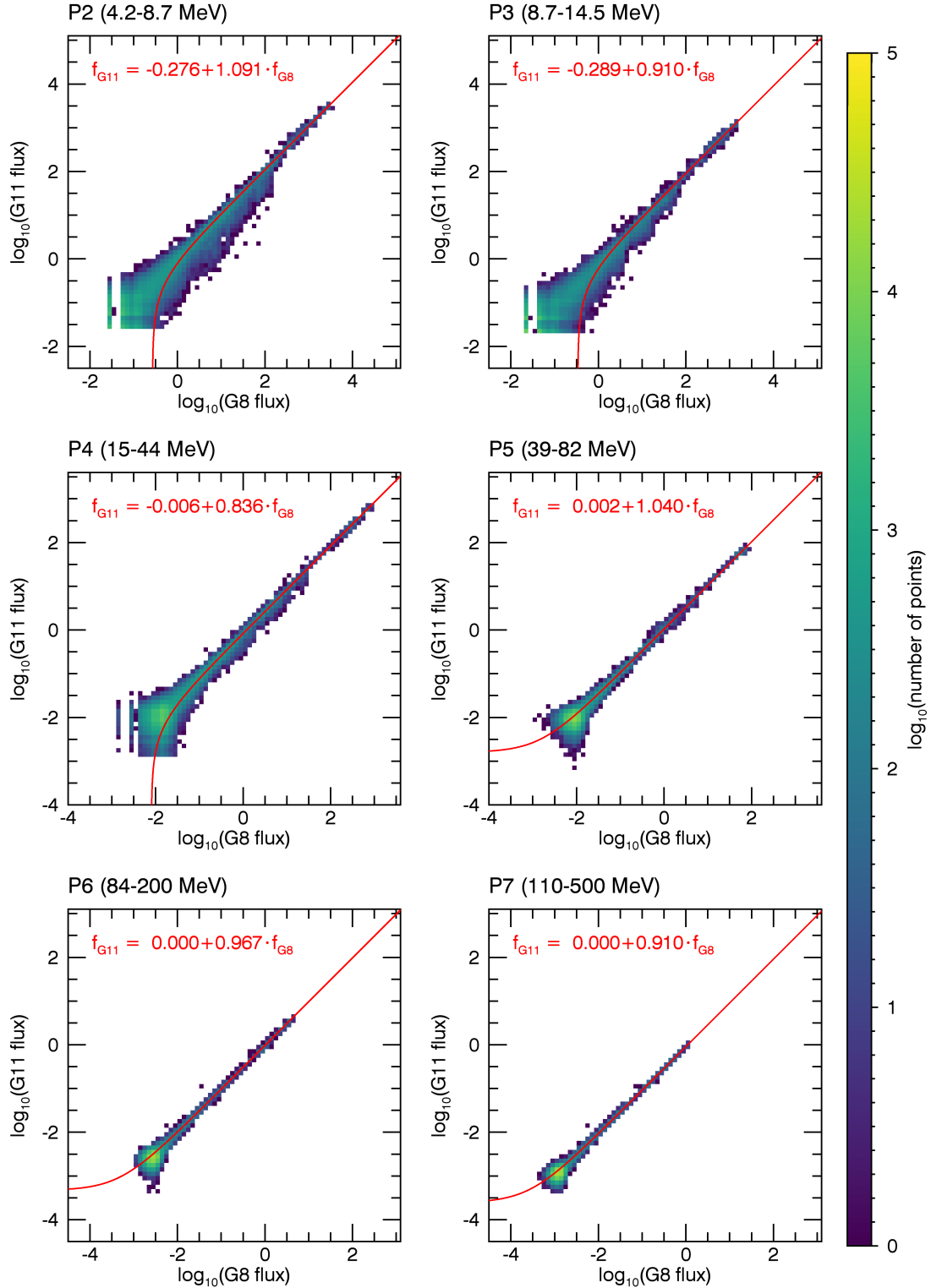


Fig. 2. Comparison of logarithms of differential fluxes in channels P2–P7 of GOES-8 (horizontal axis) and GOES-11 (vertical axis). The linear fits and their equations are shown in red (see text for details).

P5 and P7, and extrapolating that up to infinity (see Appendix C for details); however, if the resulting value, $\gamma_{P5,P7} - 0.86$, happened to be smaller than 1.5, it was replaced with 1.5 in order to avoid unrealistically hard spectra. In the case of zeros or negative flux values caused by the background subtraction, the next closest channel with a positive value was used in calculating the power law, and the range between the lower and upper energy limits of the non-positive-valued channel was excluded from the

integration. If fewer than two differential channels had positive-valued fluxes, all integral channels for that hour were assigned zero fluxes. Statistical errors of the differential fluxes were propagated into the integral fluxes, including the contributions from background subtraction and intercalibration.

Figure 3 shows a comparison between the logarithms of the calculated integral fluxes f_{10} , f_{30} , f_{60} , and f_{100} and the ones provided in the data products for GOES-8, 10, 11, and 15 for the

Table 1. Energies and geometric factors for GOES EPS/EPEAD channels P2–P7.

Channel	Energy range ^(a) (MeV)	Eff. energy (MeV)	<i>GdE</i>	
			1st gen. data processing ^(b) (cm ² sr MeV)	This study ^(a) (cm ² sr MeV)
P2	4.2–8.7	5.916	0.252	0.252
P3	8.7–14.5	11.11	0.325	0.325
P4	15–44	24.53	6.09	4.64
P5	39–82	55.29	20.0	15.5
P6	84–200	125.7	136.0	90.0
P7	110–500	214.9	891.0	300.0

Notes. ^(a)Rodriguez et al. (2017). ^(b)<https://satdat.ngdc.noaa.gov/sem/goes/software/part.txt>.

Table 2. Sources of data used to create a dataset covering the time period from 1984 to 2019.

1984-01-01–1984-12-31	GOES-5 (3s)
1985-01-01–1985-01-31	GOES-6 (3s)
1985-02-01–1985-11-30	GOES-5 (3s)
1985-12-01–1985-12-31	GOES-6 (3s)
1986-01-01–1986-12-31	GOES-5 (3s)
1987-01-01–1987-02-28	GOES-7
1987-03-01–1987-03-31	GOES-6 (3s)
1987-04-01–1991-10-14	GOES-7
1991-10-15–1991-10-31	GOES-6 (3s)
1991-11-01–1994-12-31	GOES-7
1995-01-01–2003-03-31	GOES-8
2003-04-01–2003-05-14	GOES-10
2003-05-15–2003-06-14	GOES-8
2003-06-15–2003-06-30	GOES-10
2003-07-01–2010-12-31	GOES-11
2011-01-01–2019-12-31	GOES-15

selected times given in Table 2. GOES-7 is not included in this comparison since the calculated integral fluxes are not expected to agree well with the ones provided in the data, because of the change of the geometric factor described above. As shown by the linear fits in the figure, the calculated f_{10} and f_{30} fluxes are lower than those provided in the data products, whereas the opposite is true for f_{60} and f_{100} . Using the more commonly used geometric means as effective channel energies would yield slightly higher integral fluxes for the lower energies, but clearly higher fluxes for the higher energies, resulting in a greater spectral difference. Therefore, the differences between the calculated integral fluxes and those provided in the data must result from our omission of channels P4 and P6, and properties of the Z89 algorithm such as contamination correction and different energy ranges in the integral flux calculation (see Table A5 in Rodriguez et al. 2017).

2.3. Integral SEP fluences

Before calculating the annual integral SEP fluences, all remaining data gaps in the compiled (see Table 2) one-hour differential and integral datasets were filled with logarithmically interpolated values. SEP event periods for each of the calculated integral fluxes f_{10} , f_{30} , f_{60} , f_{100} , and f_{200} were then selected using the following criteria: the non-background-subtracted one-hour differential flux had to exceed the background by more than two times the statistical error of the background for at least six consecutive hours simultaneously in the channels above and

below the integral energy; the maximum background-subtracted one-hour differential flux in the P2 channel had to exceed $0.1 \text{ cm}^{-2} \text{ sr}^{-1} \text{ s}^{-1} \text{ MeV}^{-1}$ during the event; at least 50% of the event was observed (i.e. not interpolated data gaps); and any period fulfilling the three previous event conditions at threshold energy E_i was also marked as an event at all integral energies below E_i . In order to capture as much of the SEP fluence as possible, these criteria were set very loose.

Figure 4 shows the integral flux time series covering the full time period from 1984 to 2019 for f_{10} , f_{30} , f_{60} , f_{100} , and f_{200} . SEP event fluxes are shown in green and the residual background in grey. As the integral fluxes were calculated using background-subtracted differential fluxes, the grey points are purely noise, with no visible solar cycle dependence. The fluxes, along with error estimates and flags indicating whether they belong to an SEP event or not, are available in a machine-readable format at the CDS.

Figure 5 compares the integral fluences of SEP events calculated here with those published in Goswami et al. (1988) (red plus-symbols) and Feynman et al. (1990) (blue x-symbols), which are cited as data sources in the well-known survey of historical SEP events published by Shea & Smart (1990). Furthermore, comparison with the R-ESC catalogue version 2.0⁴ is shown by grey y-symbols. Our results are shown on the vertical axis and the previously published results on the horizontal axis. In some cases the differences are quite large; for example, Feynman et al. (1990) report the fluence of the event of 24 April 1985 as 4.7 times higher for F_{10} and 2.2 times higher for F_{30} . On average, both Goswami et al. (1988) and Feynman et al. (1990) report higher fluences for F_{10} , but for F_{30} , our results tend to be higher than those in Goswami et al. (1988) and the R-ESC catalogue. The comparison for Goswami et al. (1988) and Feynman et al. (1990) includes the largest events of 1984–1986, and most events appear in both references, but with different integration times. It should also be noted that only the dates of the event onsets are given in the references, not the exact onset times; therefore, the start of integration time in all events was assumed to be the beginning of the day of the event. In the case of the R-ESC catalogue, the comparison includes all of the events of 1997–2017, for which all of the integral fluences up to F_{100} are given in the catalogue.

3. Results

Table D.1 presents the annual integral solar proton fluences F_{10} , F_{30} , F_{60} , F_{100} , and F_{200} , and their error estimates for the years

⁴ Available at <https://swe.ssa.esa.int/utu-srl-federated>; originally described in Paassilta et al. (2017).

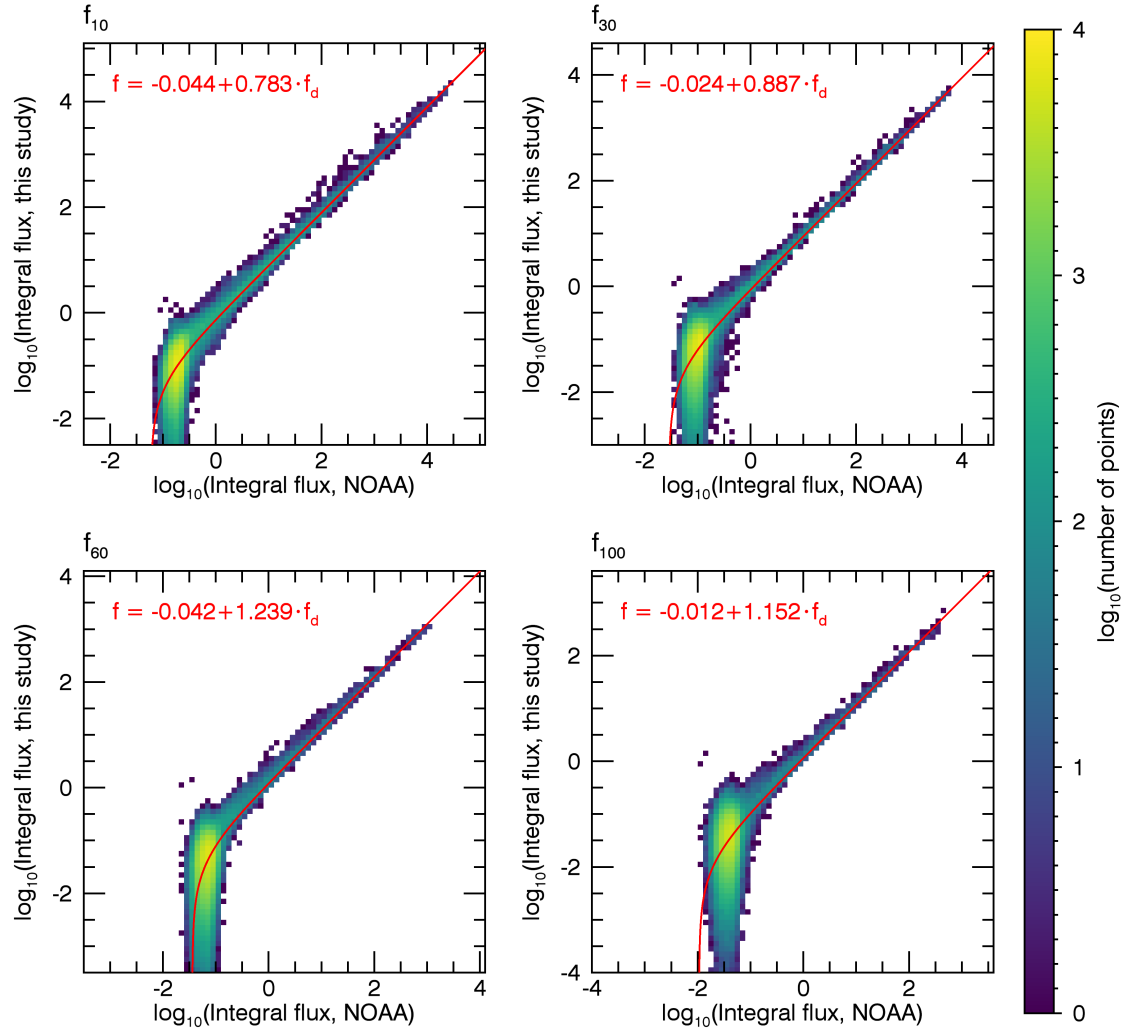


Fig. 3. Comparison between the logarithms of the calculated one-hour integral fluxes (vertical axes) and the one-hour averages of the integral fluxes provided in the data product (horizontal axes) for selected times of GOES-8–15 observations (see text for details). Linear fits and their equations are shown in red.

1984–2019. The error estimates are calculated as the statistical errors of the hourly integral fluxes, including contributions from background subtraction and intercalibration, added in quadrature. This table is also available in a machine-readable format at the CDS.

Graphical representations of the annual fluences evolution are shown in Fig. 6a for F_{30} , F_{100} , and F_{200} fluences. One can see that individual years are highly uneven in the sense of SEP fluence. Figure 6b depicts the fluence accumulation over individual solar cycles (see also Table 3). For example, 1989 provided the greatest annual fluence that dominated the entire solar cycle 22, contributing 80–90% of the cycle fluence. On the other hand, for cycle 23, the fluence was more or less evenly distributed over the years 2000–2006, leading to a gradual fluence accumulation. It is also seen that cycle 24 was a factor of 5–8 weaker, in the sense of SEP fluence, than the previous two cycles.

Annual fluences listed in Table D.1 can be presented in the form of the complementary cumulative distribution function (CCDF) $P(F)$, which gives the probability of the fluence greater than a given value F occurring in a randomly selected year. The CCDFs for the four fluences considered here are shown in Fig. 7 as open circles with error bars. Error bars correspond to the 68% confidence interval calculated for the Poisson distribution (see details in Usoskin & Kovaltsov 2012). The distributions have

smooth shapes that are neither exponential nor power law, but depict a sharp roll-off at large-fluence years probability. Quite often such CCDF shapes are described by the integral Weibull distribution (Weibull 1951; Gopalswamy 2018):

$$P = \exp(-(F/\lambda)^\kappa), \quad (3)$$

where λ and κ are the parameters of the distribution. First we checked that this shape could reasonably well describe the obtained CCDFs. Equation (3) can be easily linearised by the following replacement of variables:

$$y = \kappa \cdot x + b, \quad (4)$$

where $y = \ln(-\ln(P))$, $x = \ln(F)$, and $b = -\kappa \cdot \ln(\lambda)$. Thus, a linear relationship between y and x would imply a Weibull-shaped CCDF. These relationships are shown as insets in each panel of Fig. 7. One can see that they are nearly perfectly linear giving a solid ground to the Weibull-shape fitting. The best-fit Weibull distributions and their 68% confidence intervals are shown as dashed red curves and the red shaded area, respectively. The best-fit parameters are listed in Table 4 together with their uncertainties. The confidence-interval and parameter uncertainties were computed by a Monte Carlo method similarly to Koldobskiy et al. (2021), so that, for each realization, exact values of P and F were randomly picked, applying the normal

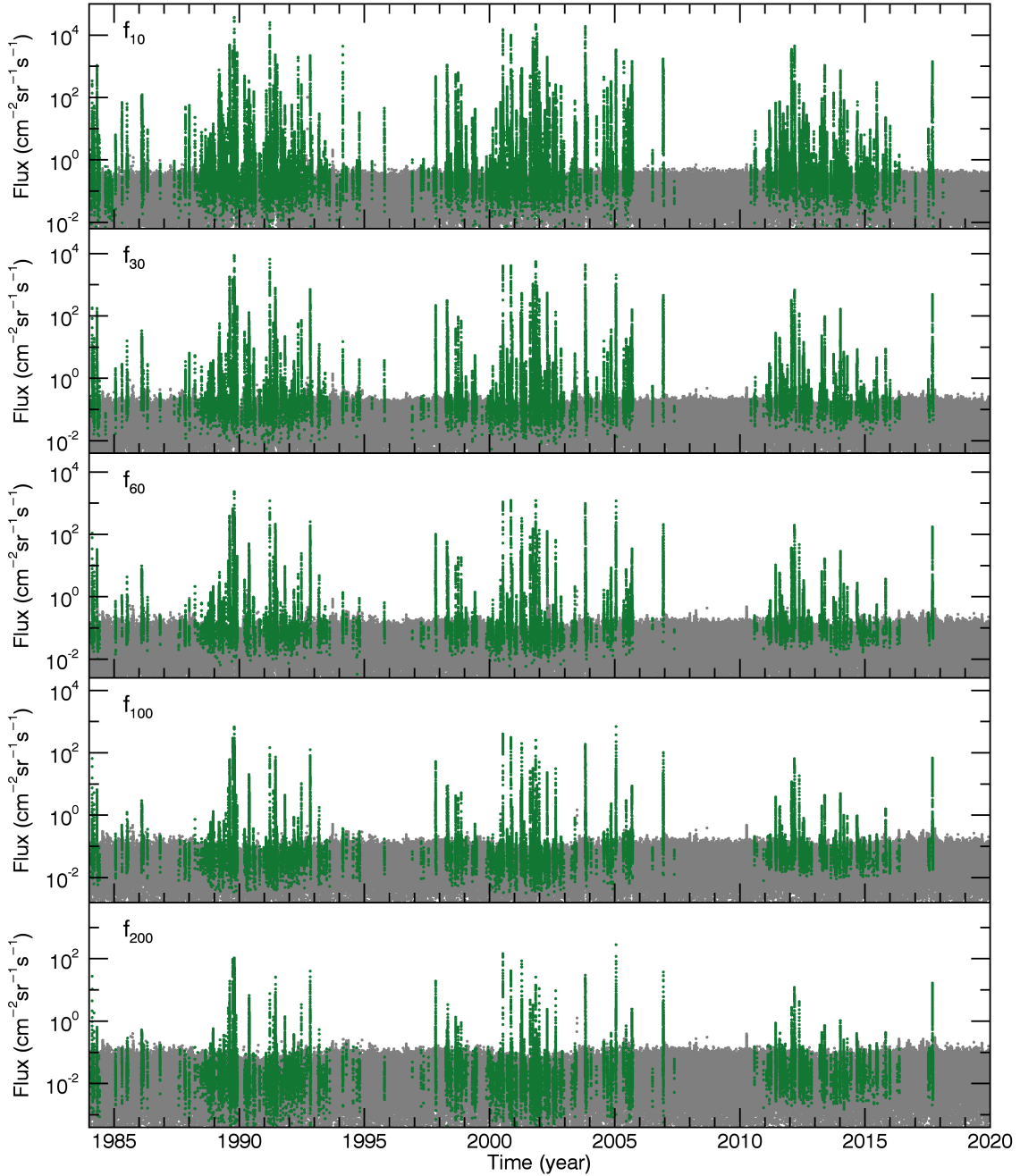


Fig. 4. Integral flux time series for the time period from 1984 to 2019 for f_{10} , f_{30} , f_{60} , f_{100} , and f_{200} , respectively, from *top to bottom*. Event periods are shown in green (see text for details).

distribution, from the confidence intervals, re-sorted, and then the fitting Weibull distribution was reconstructed using Eq. (4). For each realization, the χ^2 statistics were calculated and stored. This operation was repeated 10000 times, and finally, we constructed the distributions of χ^2 as a function of the parameters. Using these distributions, we identified the best-fit (χ^2_{\min}) and corresponding 68% confidence intervals for the parameters as bounded by the $\chi^2 = \chi^2_{\min} + 2.30$ (Press et al. 2007).

As seen from Fig. 7, the Weibull distribution perfectly describes the obtained CCDFs, except the lower and upper bounding points. The lower bounds correspond to the years (1996, 2007, 2010, and 2016) with small SEP fluences around solar cycle minima, as for example, the left-most points in the inset in panel a drops off the linear relation. The data for low-fluence years may suffer from an unclear definition above

the background, as reflected by high uncertainties, which can exceed most probable values (see Table D.1). On the other hand, the year 1989 with the largest fluence also drops off the distribution for higher energies, in other words F_{100} and F_{200} . This may be related to a small-number statistic; while years with such high fluence would have been expected to appear once per 70–100 yr, one year might have accidentally appeared during the 36-year measured interval, as indicated by the fact that the 68% confidence intervals for F_{100} and F_{200} overlap with those for the best-fit distribution.

4. Conclusions

We reconstructed the annual SEP fluences (see Table D.1) in five energy ranges, that is, above 10, 30, 60, 100, and 200 MeV

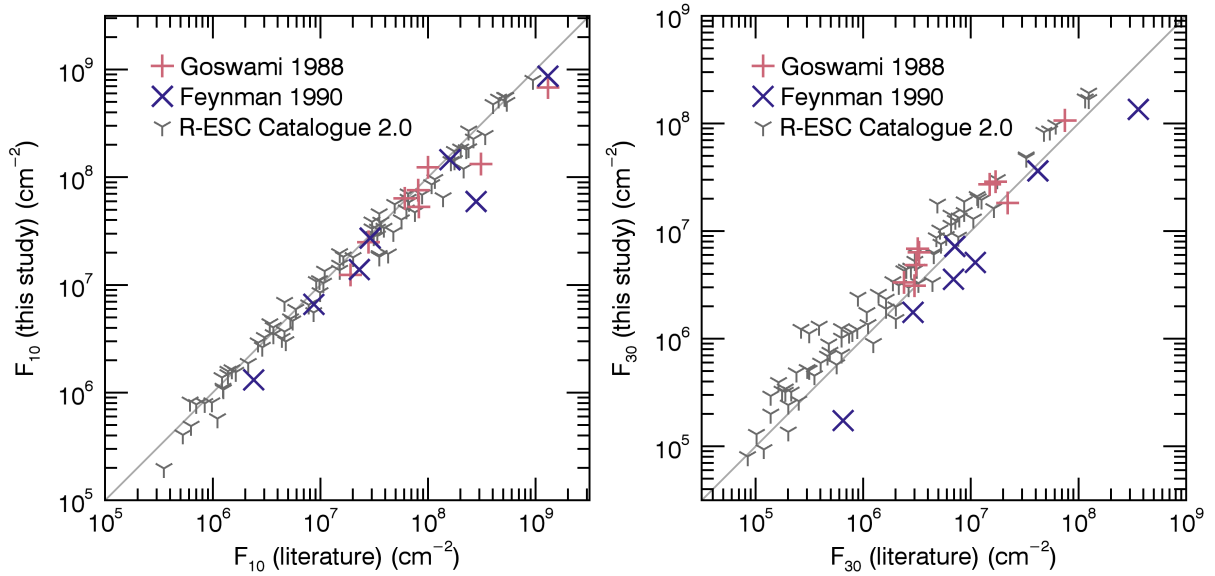


Fig. 5. Comparison of fluences of individual SEP events occurring during 1984–1986 for F_{10} (left panel) and F_{30} (right panel). Event fluences calculated in this study are plotted on the vertical axis and the corresponding fluences reported in Goswami et al. (1988) (red plus-symbols), Feynman et al. (1990) (blue x-symbols) and the R-ESC-catalogue (grey y-symbols) are plotted on the horizontal axis.

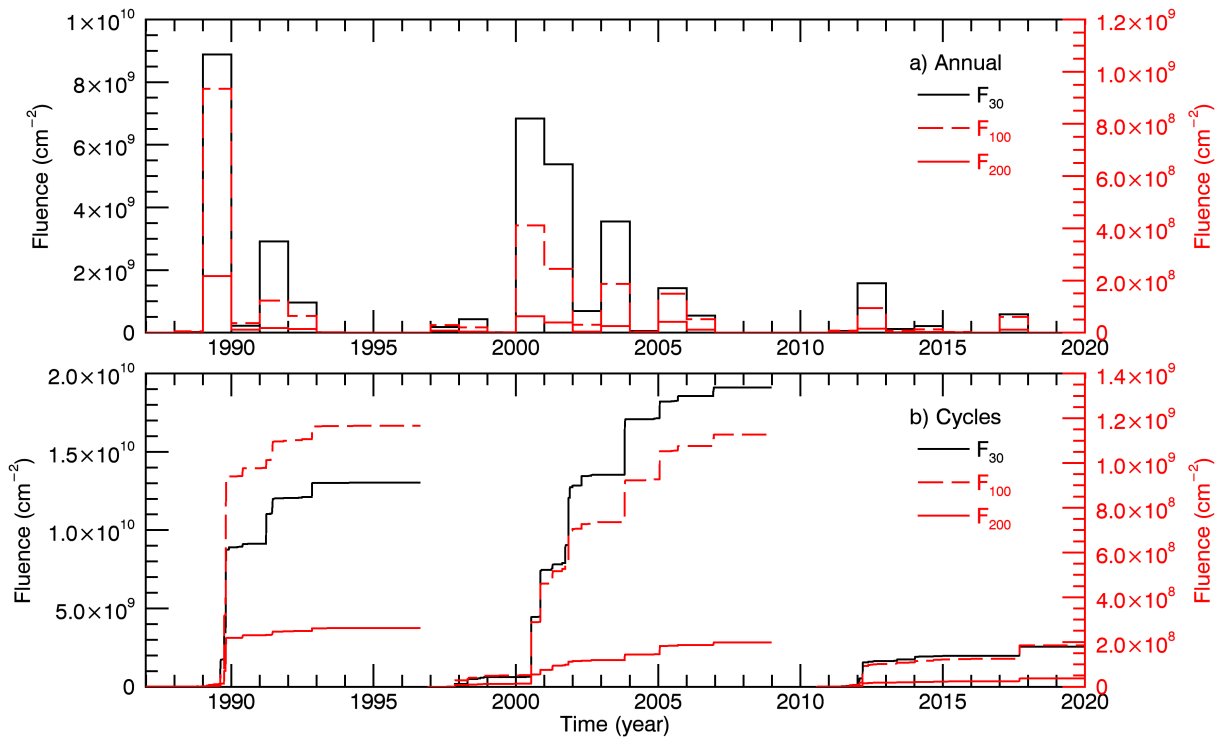


Fig. 6. Time evolution of F_{30} (black curves, left Y-axis), F_{100} (red dashed curves, right Y-axis), and F_{200} (red solid curves, right Y-axis) fluences. Panel a depicts the annual fluences as listed in Table D.1. Panel b depicts the cumulative fluences for solar cycles 22, 23, and 24. Error bars are not shown.

Table 3. Solar cycle integrated solar proton fluences and their statistical errors for cycles 22–24.

Solar cycle	F_{10}	$\sigma_{F_{10}}$	F_{30}	$\sigma_{F_{30}}$	F_{60}	$\sigma_{F_{60}}$	F_{100}	$\sigma_{F_{100}}$	F_{200}	$\sigma_{F_{200}}$
22	5.00×10^{10}	1.05×10^9	1.30×10^{10}	2.29×10^8	3.65×10^9	6.17×10^6	1.17×10^9	2.01×10^6	2.62×10^8	1.50×10^6
23	7.81×10^{10}	6.03×10^8	1.91×10^{10}	7.06×10^7	4.54×10^9	8.34×10^6	1.13×10^9	2.72×10^6	1.98×10^8	1.99×10^6
24	1.39×10^{10}	3.12×10^8	2.57×10^9	1.55×10^7	6.31×10^8	4.47×10^6	1.85×10^8	1.93×10^6	3.67×10^7	1.77×10^6

Notes. All fluence and error values are in units of cm^{-2} .

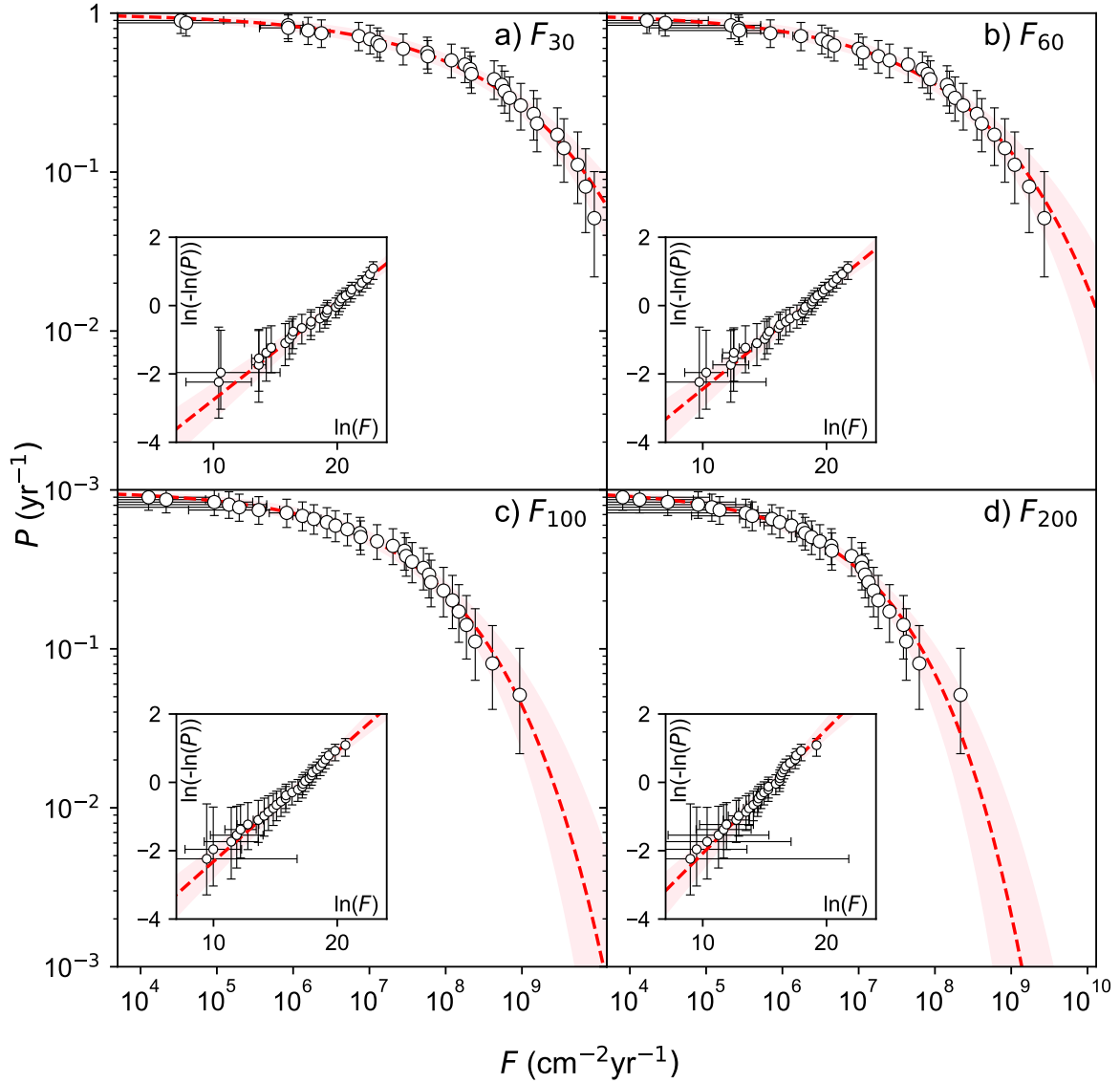


Fig. 7. Complementary cumulative distribution functions (CCDFs) of years with the value of the annual fluence exceeding the given value F for four energy values discussed here, F_{30} , F_{60} , F_{100} , and F_{200} , as shown in *panels a through d*, respectively. The dots correspond to the F values from Table D.1, and the probability P and its 68% confidence-level uncertainty are calculated for the Poisson distribution. The red dashed lines with red shading depict the best-fit Weibull distributions and their 68% confidence-level uncertainties, respectively. The insets depict the $\ln(-\ln(P))$ -vs.- $\ln(F)$ dependence, which should be linear for the Weibull distribution (see text).

Table 4. Parameters of the best-fit Weibull distribution for the CCDF of annual F_{30} , F_{60} , F_{100} , and F_{200} .

Parameter	F_{30}	F_{60}	F_{100}	F_{200}
κ	$0.29^{+0.05}_{-0.04}$	$0.29^{+0.05}_{-0.05}$	$0.32^{+0.06}_{-0.05}$	$0.36^{+0.07}_{-0.06}$
λ (cm^{-2})	$(3.50^{+1.45}_{-1.01}) \times 10^8$	$(9.18^{+3.68}_{-2.59}) \times 10^7$	$(2.92^{+1.03}_{-0.77}) \times 10^7$	$(6.73^{+2.06}_{-1.56}) \times 10^6$

for the period from 1984–2019, using the revisited calibration of in situ data obtained on board the GOES-family spacecraft. These fluences, as well as time series of integral SEP fluxes f_{10} , f_{30} , f_{60} , f_{100} , and f_{200} at one-hour resolution, are provided at the CDS. The annual fluences vary over a solar cycle with the maximum occurrence around cycle maximum phase. It is found that the SEP accumulated fluences during solar cycle 24 were significantly (a factor of 5–7) smaller than during the previous cycles 22 and 23. The solar-cycle fluence is accumulated

mostly during strong SEP events, for instance 70–90% of the fluence for cycle 22 was accumulated during a series of strong SEP events in the Autumn of 1989. CCDFs of the annual fluences (Fig. 7) depict a fast roll-off for high values of the fluences and are almost perfectly described by the Weibull-distribution shape (Eq. (3)). This suggests that the distribution can be extrapolated to extremely high fluences, typical for historical events (e.g. Usoskin 2017). In particular, the years with SEP fluences an order of magnitude greater than the ones observed during the

last 45 years are unlikely to be occur on the millennial timescale. This can be combined with the statistic of extreme solar particle events recorded with cosmogenic isotopes throughout the Holocene (Usoskin & Kovaltsov 2021).

Finally, the improved hourly proton fluxes presented in this paper will enhance the accuracy of products relying on statistical proton models, such as those in the frame of the ESA Space Safety Programme's network of space weather service development and pre-operational activities, as well as those already being provided by the Space Radiation Expert Service Centre on the European Space Agency Space Weather Service (ESA SWE) portal as a federated product⁵.

Acknowledgements. The work has been conducted as a part of the activities of the Expert Group UTU/SRL of the Radiation Expert Service Centre of ESA. R.V. acknowledges funding from the Academy of Finland (FORESAIL Centre of Excellence, project no. 336809). This work was also partly supported by the Academy of Finland (projects ESPERA, No. 321882, and QUASARE, No. 330064), University of Oulu (Project SARPEDON). I.U. has benefited from discussions on the topic during the ISSI SEESUP team work.

References

- Atwell, W., Tylka, A. J., Dietrich, W. F., Rojdev, K., & Matzkind, C. 2015, in *Proceedings of the 45th International Conference on Environmental Systems*, Bellevue, WA, USA
- Bazilevskaya, G. A., Cliver, E. W., Kovaltsov, G. A., et al. 2014, *Space Sci. Rev.*, **186**, 409
- Bruno, A. 2017, *Space Weather*, **15**, 1191
- Cohen, C. M. S., & Mewaldt, R. A. 2018, *Space Weather*, **16**, 1616
- Desai, M., & Giacalone, J. 2016, *Living Rev. Sol. Phys.*, **13**, 3
- Efron, B., & Tibshirani, R. 1986, *Stat. Sci.*, **1**, 54
- Feynman, J., & Gabriel, S. B. 2000, *J. Geophys. Res.*, **105**, 10543
- Feynman, J., Armstrong, T. P., Dao-Gibner, L., & Silverman, S. 1990, *J. Spacecr. Rockets*, **27**, 403
- Feynman, J., Spitale, G., Wang, J., & Gabriel, S. 1993, *J. Geophys. Res.*, **98**, 13
- Firoz, K. A., Cho, K.-S., Hwang, J., et al. 2010, *J. Geophys. Res.*, **115**, A09105
- Gopalswamy, N. 2018, in *Extreme Events in Geospace*, ed. N. Buzulukova (Elsevier), 37
- Goswami, J. N., McGuire, R. E., Reedy, R. C., Lal, D., & Jha, R. 1988, *J. Geophys. Res.*, **93**, 7195
- Grubb, R. N. 1975, *The SMS/GOES space environment monitor subsystem*, Tech. Rep. NOAA Technical Memorandum ERL SEL-42, Boulder, Colorado, USA
- Hanser, F. A. 2011, *EPS/HEPAD Calibration and Data Handbook*, Tech. Rep. GOESN-ENG-048, Assurance Technology Corporation, Carlisle, MA
- Hu, S., & Semones, E. 2022, *J. Space Weather Space Clim.*, **12**, 5
- Jiggins, P. T. A., Gabriel, S. B., Heynderickx, D., et al. 2012, *IEEE Trans. Nucl. Sci.*, **59**, 1066
- Jiggins, P., Chavy-Macdonald, M., Santin, G., et al. 2014, *J. Space Weather Space Clim.*, **4**, A20
- Jiggins, P., Heynderickx, D., Sandberg, I., et al. 2018, *J. Space Weather Space Clim.*, **8**, A31
- Jun, I., Swimm, R. T., Ruzmaikin, A., et al. 2007, *Adv. Space Res.*, **40**, 304
- King, J. H. 1974, *J. Spacecr. Rockets*, **11**, 401
- Klein, K.-L., & Dalla, S. 2017, *Space Sci. Rev.*, **212**, 1107
- Koldobskiy, S. A., Raukunen, O., Vainio, R., Kovaltsov, G., & Usoskin, I. 2021, *A&A*, **647**, A132
- Koldobskiy, S. A., Usoskin, I., & Kovaltsov, G. 2022, *J. Geophys. Res. Space Phys.*, **127**, e2021JA029919
- Kovaltsov, G. A., Usoskin, I. G., Cliver, E. W., Dietrich, W. F., & Tylka, A. J. 2014, *Sol. Phys.*, **289**, 4691
- Kress, B. T., Rodriguez, J. V., & Onsager, T. G. 2020, in *The GOES-R Series*, eds. S. J. Goodman, T. J. Schmit, J. Daniels, & R. J. Redmon, 243
- Kress, B. T., Rodriguez, J. V., Boudouridis, A., et al. 2021, *Space Weather*, **19**, e02750
- Lafferty, G. D., & Wyatt, T. R. 1995, *Nucl. Instrum. Methods Phys. Res., Sect. A*, **355**, 541
- Mewaldt, R. A.,Looper, M. D., Cohen, C. M. S., et al. 2012, *Space Sci. Rev.*, **171**, 97
- Mewaldt, R. A., Cohen, C. M. S., Mason, G. M., et al. 2015, in *Proceedings of the 34th International Cosmic Ray Conference*, The Hague, The Netherlands
- Onsager, T., Grubb, R., Kunches, J., et al. 1996, in *GOES-8 and Beyond*, ed. E. R. Washwell, *Proceedings of SPIE*, Denver, Colorado, USA, 281
- Paassilta, M., Raukunen, O., Vainio, R., et al. 2017, *J. Space Weather Space Clim.*, **7**, A14
- Panametrics, Inc. 1979, GOES D, E, F Progress Report, *Energetic Particle Sensor Telescope Calibration Work*, Tech. Rep. PANA-GOESP-CR2, Panametrics, Inc., Waltham, MA
- Panametrics, Inc. 1980, GOES D, E, F Progress Report, *Energetic Particle Sensor Dome Calibration Work*, Tech. Rep. PANA-GOESP-CR3, Panametrics, Inc., Waltham, MA
- Panametrics, Inc. 1995, *Calibration Report for the EPS Dome Sensor Response to Protons*, Tech. Rep. NXT-CAL-102, Panametrics, Inc., Waltham, MA
- Papaioannou, A., Sandberg, I., Anastasiadis, A., et al. 2016, *J. Space Weather Space Clim.*, **6**, A42
- Poluianov, S., Kovaltsov, G. A., & Usoskin, I. G. 2018, *A&A*, **618**, A96
- Press, W., Teukolsky, S., Vetterling, W., & Flannery, B. 2007, *Numerical Recipes: The Art of Scientific Computing*, 3rd edn. (USA: Cambridge University Press)
- Raukunen, O., Vainio, R., Tylka, A. J., et al. 2018, *J. Space Weather Space Clim.*, **8**, A04
- Raukunen, O., Paassilta, M., Vainio, R., et al. 2020, *J. Space Weather Space Clim.*, **10**, 24
- Reames, D. V. 2013, *Space Sci. Rev.*, **175**, 53
- Reedy, R. 1998, *Proc. Indian Acad. Sci., Earth Planet. Sci.*, **107**, 433
- Reedy, R. C. 2012, in *43rd Lunar and Planetary Science Conference*, The Woodlands, Texas, USA, 1285
- Reedy, R. C. 2014, in *45th Annual Lunar and Planetary Science Conference*, Lunar and Planetary Science Conference, 2324
- Robinson, Z. D., Adams, J. H., Xapsos, M. A., & Stauffer, C. A. 2018, *J. Space Weather Space Clim.*, **8**, A24
- Rodriguez, J. V., Krosschell, J. C., & Green, J. C. 2014, *Space Weather*, **12**, 92
- Rodriguez, J. V., Sandberg, I., Mewaldt, R. A., Daglis, I. A., & Jiggins, P. 2017, *Space Weather*, **15**, 290
- Rosenqvist, L., Hilgers, A., Evans, H., et al. 2005, *J. Spacecr. Rockets*, **42**, 1077
- Sandberg, I., Jiggins, P., Heynderickx, D., & Daglis, I. A. 2014, *Geophys. Res. Lett.*, **41**, 4435
- Sauer, H. H. 1993, in *Proceedings of the 23rd International Cosmic Ray Conference*, eds. D. A. Leahy, R. B. Hicks, & D. Venkatesan, Vol. 3, Calgary, Canada, 250
- Sellers, F. B., & Hanser, F. A. 1996, in *GOES-8 and Beyond*, ed. E. R. Washwell, *Proceedings of SPIE*, Denver, Colorado, USA, 353
- Shea, M., & Smart, D. 1992, *Radiocarbon*, **34**, 255
- Shea, M. A., & Smart, D. F. 1990, *Sol. Phys.*, **127**, 297
- Smart, D., & Shea, M. 2002, *Adv. Space Res.*, **30**, 1033
- Tylka, A. J., & Dietrich, W. F. 2009, in *Proceedings of the 31st International Cosmic Ray Conference*, eds. M. Giller, & J. Szabelski, Łódź, Poland
- Tylka, A. J., & Lee, M. A. 2006, *ApJ*, **646**, 1319
- Tylka, A. J., Cohen, C. M. S., Dietrich, W. F., et al. 2005, *ApJ*, **625**, 474
- Usoskin, I. G. 2017, *Living Rev. Sol. Phys.*, **14**, 3
- Usoskin, I. G., & Kovaltsov, G. A. 2012, *ApJ*, **757**, 92
- Usoskin, I., & Kovaltsov, G. 2021, *Geophys. Res. Lett.*, **48**, e94848
- Usoskin, I., Koldobskiy, S., Kovaltsov, G. A., et al. 2020, *A&A*, **640**, A17
- Vainio, R., Desorgher, L., Heynderickx, D., et al. 2009, *Space Sci. Rev.*, **147**, 187
- Van Allen, J. A., Baker, D. N., Randall, B. A., & Sentman, D. D. 1974, *J. Geophys. Res.*, **79**, 3559
- Washwell, E. R., ed. 1996, *GOES-8 and Beyond*, *Proceedings of SPIE*, Denver, Colorado, USA
- Weibull, W. 1951, *J. Appl. Mech.*, **18**, 293
- Xapsos, M. A., Summers, G. P., Barth, J. L., Stassinopoulos, E. G., & Burke, E. A. 2000, *IEEE Trans. Nucl. Sci.*, **47**, 486
- Xapsos, M. A., Stauffer, C., Barth, J. L., & Burke, E. A. 2006, *IEEE Trans. Nucl. Sci.*, **53**, 1839

⁵ <https://swe.ssa.esa.int/utu-sr1-federated>

Appendix A: Geometric factor of the first GOES generation

Differential particle fluxes in the GOES datafiles are given in units of $\text{cm}^{-2} \text{sr}^{-1} \text{s}^{-1} \text{MeV}^{-1}$, in other words, particle counts divided by the geometry-energy factor GdE (in units of $\text{cm}^2 \text{sr MeV}$) and the accumulation time t (in units of s). The GdE values are not included in the GOES data files, and various different values can be found in the literature (e.g. Panametrics, Inc. 1979, 1980, 1995; Sauer 1993; Sellers & Hanser 1996; Rodriguez et al. 2014). In addition, neither the counts nor the accumulation times are included in the original data files. This makes it practically impossible to find out the values of GdE that have been used to calculate the fluxes.

However, the 3s data files contain ‘Data points per average’-columns for each channel, which allows a selection of datapoints based on the accumulation time. By selecting observations which were averaged from 12 samples in the channels P2-P5, and 24 samples in P6-P7, with 24.5 seconds per sample for P2-P5 and 12.25 seconds per sample for P6-P7 (Grubb 1975), and assuming 50% duty cycle as for GOES 8-12 (Rodriguez et al. 2014), we get the accumulation time $t = 147$ s. Therefore, with the equation relating counts and fluxes, $c = f \cdot GdE \cdot t$, knowing the flux f and accumulation time t , we can find out the

value of GdE , knowing that the equation must result in integer values for the counts c .

This way we were able to find the values that have been used in the NOAA data processing for the first GOES generation. The results are given in Table 1; the values for channels P2 and P3 the agree with most published values, the value for P4 agree with those of Panametrics, Inc. (1979, 1980) and Sauer (1993), but the values for P5–P7 do not agree with any previous publications that we are aware of. However, the results of all channels are equal to the geometric factors listed in NOAA’s example data file at <https://satdat.ngdc.noaa.gov/sem/goes/software/part.txt>.

Appendix B: Linear relationship between overlapping GOES datasets

The relationships between pairs of overlapping GOES observations were quantified with linear fits of the form $f_y = a + bf_x$, calculated with the least absolute deviation (LAD) method. Tables B.1 and B.2 present the values of the slope b and intercept a , respectively, for all overlapping pairs. Error estimates σ_b and σ_a , calculated with the bootstrap method (e.g. Efron & Tibshirani 1986), are also given in the tables.

Table B.1. Slopes b and their errors σ_b in the linear fits $f_y = a + bf_x$ to overlapping measurements of two GOES satellites

Satellite		P2		P3		P4		P5		P6		P7	
x	y	b	σ_b	b	σ_b	b	σ_b	b	σ_b	b	σ_b	b	σ_b
G05	G05 (3s)	1.000	0.000	1.000	0.000	1.000	0.000	1.000	0.000	1.000	0.000	0.999	0.000
G05	G06	1.052	0.004	0.724	0.003	0.149	0.001	0.889	0.004	1.017	0.001	1.017	0.001
G05	G06 (3s)	1.054	0.004	0.725	0.003	0.149	0.001	0.893	0.002	1.014	0.000	1.010	0.001
G05 (3s)	G06	1.053	0.004	0.723	0.003	0.149	0.001	0.886	0.003	1.017	0.001	1.018	0.000
G05 (3s)	G06 (3s)	1.060	0.003	0.725	0.002	0.146	0.001	0.890	0.004	1.017	0.000	1.013	0.001
G06	G06 (3s)	1.000	0.000	1.000	0.000	1.000	0.000	1.000	0.000	1.000	0.000	1.000	0.000
G06	G07	0.903	0.003	1.246	0.005	4.375	0.038	0.714	0.001	0.749	0.002	1.039	0.002
G06	G07 (3s)	0.911	0.003	1.243	0.005	4.372	0.048	0.717	0.002	0.750	0.002	1.033	0.003
G06 (3s)	G07	0.914	0.004	1.245	0.005	4.332	0.059	0.717	0.001	0.752	0.002	1.032	0.003
G06 (3s)	G07 (3s)	0.912	0.003	1.244	0.004	4.353	0.053	0.718	0.001	0.753	0.003	1.029	0.003
G07	G07 (3s)	1.000	0.000	1.000	0.000	1.000	0.000	1.000	0.000	1.000	0.000	1.000	0.000
G07	G08	1.233	0.024	0.833	0.022	1.795	0.034	1.344	0.002	1.052	0.001	1.021	0.001
G08	G09	1.034	0.005	0.953	0.003	0.940	0.003	1.067	0.003	1.072	0.006	0.971	0.007
G08	G10	0.823	0.013	0.668	0.007	0.781	0.007	0.823	0.005	0.968	0.004	0.901	0.003
G08	G11	1.091	0.007	0.910	0.009	0.836	0.002	1.040	0.007	0.967	0.002	0.910	0.001
G08	G12	1.015	0.006	0.763	0.006	1.026	0.008	0.973	0.003	-	-	-	-
G09	G10	0.751	0.002	0.749	0.010	0.885	0.010	0.769	0.004	0.965	0.003	0.964	0.002
G10	G11	1.144	0.009	1.152	0.009	0.995	0.007	1.198	0.006	0.995	0.003	1.000	0.002
G10	G12	1.124	0.009	1.229	0.017	1.213	0.012	1.116	0.006	-	-	-	-
G10	G13	1.455	0.014	1.211	0.016	1.398	0.015	1.151	0.006	-	-	-	-
G11	G12	1.004	0.002	1.091	0.003	1.233	0.003	0.966	0.002	-	-	-	-
G11	G13	1.091	0.005	0.954	0.004	1.301	0.002	0.918	0.001	1.064	0.003	1.039	0.003
G11	G14	0.936	0.026	0.655	0.001	0.985	0.002	0.951	0.001	1.037	0.001	1.172	0.001
G11	G15	0.750	0.006	0.664	0.020	1.011	0.003	0.889	0.002	1.004	0.002	1.100	0.001
G12	G13	1.061	0.002	0.841	0.005	1.041	0.001	0.938	0.001	-	-	-	-
G12	G14	0.793	0.064	0.655	0.011	0.792	0.002	0.961	0.002	-	-	-	-
G12	G15	0.750	0.018	0.655	0.026	0.812	0.007	0.910	0.006	-	-	-	-
G13	G14	0.866	0.013	0.740	0.025	0.958	0.008	0.985	0.001	0.939	0.000	1.029	0.000
G13	G15	0.951	0.004	1.001	0.005	0.976	0.002	0.907	0.001	0.861	0.002	0.926	0.004
G14	G15	0.677	0.021	0.804	0.017	0.838	0.007	0.950	0.000	0.932	0.000	0.948	0.000

Table B.2. Intercepts a and their errors σ_a in the linear fits $f_y = a + bf_x$ to overlapping measurements of two GOES satellites

Satellite		P2		P3		P4		P5		P6		P7	
x	y	a	σ_a	a	σ_a	a	σ_a	a	σ_a	a	σ_a	a	σ_a
G05	G05 (3s)	0.000	0.000	-0.000	0.000	-0.000	0.000	-0.000	0.000	0.000	0.000	0.000	0.000
G05	G06	-0.020	0.006	-0.000	0.008	0.046	0.001	0.002	0.000	0.000	0.000	0.000	0.000
G05	G06 (3s)	-0.026	0.008	-0.001	0.008	0.045	0.001	0.001	0.000	0.000	0.000	0.000	0.000
G05 (3s)	G06	-0.023	0.007	0.008	0.008	0.046	0.001	0.002	0.000	0.000	0.000	0.000	0.000
G05 (3s)	G06 (3s)	-0.043	0.005	0.020	0.005	0.071	0.002	0.002	0.000	0.000	0.000	0.000	0.000
G06	G06 (3s)	-0.000	0.000	-0.000	0.000	-0.000	0.000	-0.000	0.000	-0.000	0.000	-0.000	0.000
G06	G07	0.248	0.006	0.191	0.005	0.324	0.009	0.005	0.000	0.002	0.000	-0.000	0.000
G06	G07 (3s)	0.254	0.007	0.191	0.005	0.326	0.011	0.005	0.000	0.002	0.000	-0.000	0.000
G06 (3s)	G07	0.247	0.008	0.182	0.006	0.334	0.012	0.005	0.000	0.002	0.000	-0.000	0.000
G06 (3s)	G07 (3s)	0.248	0.006	0.179	0.004	0.333	0.010	0.005	0.000	0.002	0.000	-0.000	0.000
G07	G07 (3s)	-0.000	0.000	-0.000	0.000	-0.000	0.000	-0.000	0.000	-0.000	0.000	-0.000	0.000
G07	G08	0.457	0.059	0.278	0.060	0.029	0.005	0.000	0.000	0.000	0.000	0.000	0.000
G08	G09	-0.096	0.005	-0.064	0.004	0.002	0.001	-0.001	0.000	-0.000	0.000	0.000	0.000
G08	G10	-0.948	0.055	-0.580	0.021	-0.068	0.003	-0.002	0.000	0.000	0.000	0.000	0.000
G08	G11	-0.276	0.013	-0.289	0.016	-0.006	0.001	0.002	0.000	0.000	0.000	0.000	0.000
G08	G12	0.012	0.011	0.037	0.006	-0.001	0.002	0.000	0.000	-	-	-	-
G09	G10	0.000	0.000	0.000	0.000	0.000	0.000	0.000	0.000	0.000	0.000	0.000	0.000
G10	G11	1.697	0.044	0.649	0.019	0.120	0.004	-0.002	0.000	0.001	0.000	0.000	0.000
G10	G12	2.983	0.073	1.119	0.045	0.180	0.009	-0.001	0.000	-	-	-	-
G10	G13	4.325	0.472	1.546	0.121	0.237	0.043	0.001	0.001	-	-	-	-
G11	G12	0.285	0.012	0.180	0.007	0.020	0.001	0.001	0.000	-	-	-	-
G11	G13	0.031	0.010	0.028	0.007	-0.003	0.001	0.001	0.000	-0.000	0.000	0.000	0.000
G11	G14	-0.073	0.020	0.000	0.000	0.000	0.000	0.000	0.000	0.000	0.000	0.000	0.000
G11	G15	0.000	0.000	0.000	0.000	0.000	0.000	0.000	0.000	0.000	0.000	0.000	0.000
G12	G13	-0.071	0.008	0.051	0.010	-0.006	0.001	0.001	0.000	-	-	-	-
G12	G14	0.012	0.031	0.000	0.000	0.000	0.000	0.000	0.000	-	-	-	-
G12	G15	0.000	0.000	0.000	0.000	0.000	0.000	0.000	0.000	-	-	-	-
G13	G14	0.073	0.008	0.076	0.014	0.002	0.002	0.000	0.000	0.000	0.000	0.000	0.000
G13	G15	-0.032	0.005	-0.114	0.006	-0.014	0.000	0.001	0.000	0.000	0.000	0.000	0.000
G14	G15	0.123	0.014	0.064	0.010	0.002	0.001	0.000	0.000	0.000	0.000	0.000	0.000

Notes. All values are in units of $\text{cm}^{-2} \text{sr}^{-1} \text{s}^{-1} \text{MeV}^{-1}$.

Appendix C: Extrapolation of the high-energy spectrum

In most major SEP events, the proton flux measured by P6 seems to be lower than what would be expected from the fluence measured by the neighbouring channels P5 and P7. Figure C.1 shows the power law index between P5 and P7, $\gamma_{P5,P7}$, against the power law index between P6 and P7, $\gamma_{P6,P7}$, calculated for fluences of all major SEP events during 1986–2019, which were observed above background at ~ 600 MeV (channel P10 of the High-Energy Proton and Alpha Detector (HEPAD) on board the GOES satellites; see [Raukunen et al. 2020](#), for details on the bow-tie analysis). All of the points in the figure are below the dashed grey diagonal, showing that the spectrum between P6 and P7 is harder than the spectrum between P5 and P7 in all of the major events. In principle, this could be due to the effective energy of the channel P6 being estimated too low, or conversely, effective energies of channels P5 and P7 estimated too high, but this is only speculation.

In addition to causing an unrealistic downwards bend in the spectrum, this causes a problem in the flux integration: if the spectrum above P7 would be extrapolated using the power law between P6 and P7, the integral flux above P7 would be significantly overestimated. To avoid this, we decided to omit P6 altogether, and calculated the spectral extrapolation using P5 and P7.

Assuming that the spectrum above P7 would be a single power law up to infinity is not correct, since the SEP spec-

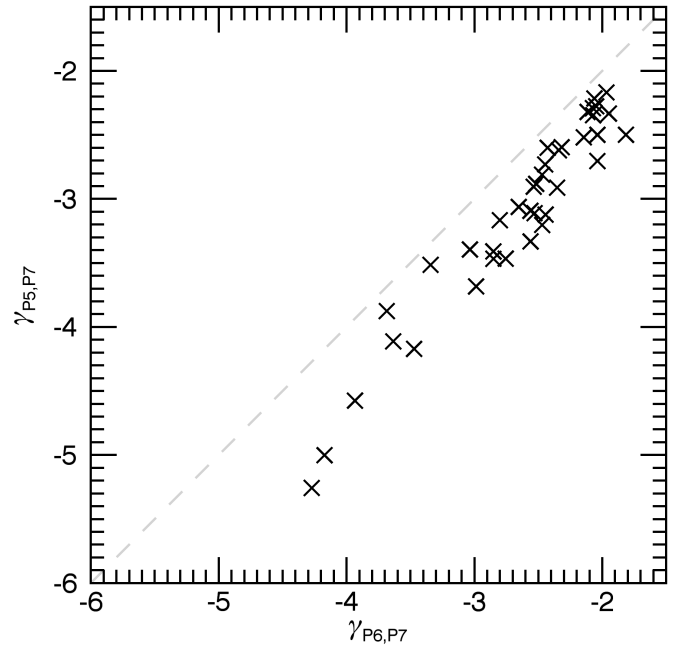


Fig. C.1. Power law index between P5 and P7, $\gamma_{P5,P7}$, as a function of the power law index between P6 and P7, $\gamma_{P6,P7}$. The diagonal is shown by a dashed grey line.

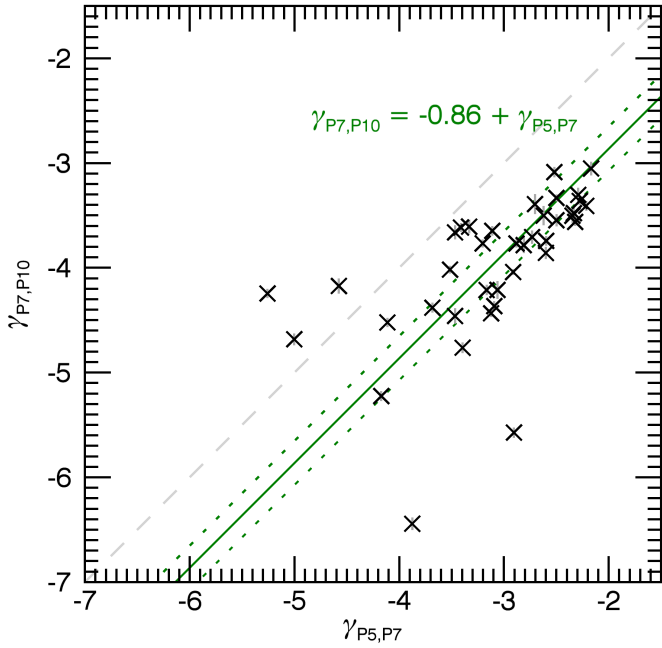


Fig. C.2. Power law index between P7 and P10, $\gamma_{P7,P10}$, as a function of the power law index between P5 and P7, $\gamma_{P5,P7}$. The diagonal is shown by a dashed grey line. The green solid line is fitted with the slope fixed at 1, and the green dashed lines show the 95% confidence interval of the fit.

tra tend to soften at high energies (e.g. Usoskin et al. 2020; Koldobskiy et al. 2021), and therefore a single power law would result in overestimation. The integral fluxes in the GOES data product have been calculated by extrapolating the P6–P7 spectrum up to 500 MeV (Rodriguez et al. 2017), but no justification for the upper limit is found in the literature. High-energy GOES/HEPAD data exist, but using them directly in the integration would not be feasible because of their high background levels. However, we can use fluences of large SEP events to calculate a relationship between the medium energy (EPS) and high-energy (HEPAD) spectral indices. Figure C.2 shows the power law index between P7 and P10, $\gamma_{P7,P10}$, as a function of the power law index between P5 and P7, $\gamma_{P5,P7}$, for the same major SEP events as the previous figure. The solid green line has a fixed slope of 1 and the intercept is calculated as the bootstrap median value of $\bar{\gamma}_{P7,P10} - \bar{\gamma}_{P5,P7}$, where $\bar{\gamma}$ denotes the mean of γ . The dashed green lines show the 95% confidence interval of the fit.

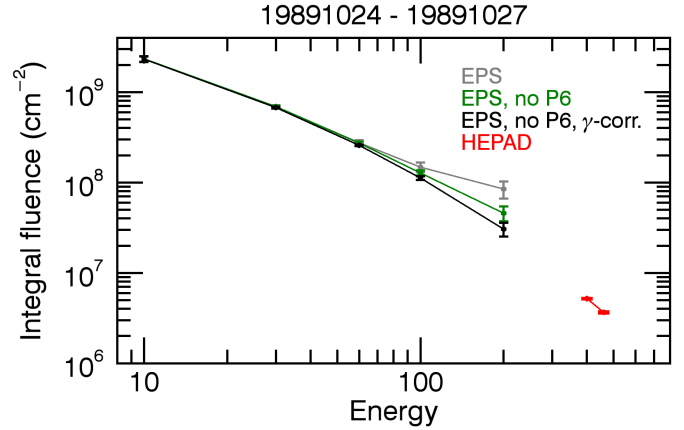


Fig. C.3. Fluence spectrum of the SEP event starting on 24 October 1989.

We used the calculated intercept, -0.86 , as a ‘correction’ in the calculation of integral fluxes above P7, namely, we extrapolated the spectrum up to infinity using a power law index $\gamma_{P7,\infty} = \gamma_{P5,P7} - 0.86$. As an example of the effect of the spectral extrapolation, Figure C.3 shows the integral fluence spectrum of the major SEP event (GLE 45), starting on 24 October 1989. The spectrum calculated by extrapolating with $\gamma_{P6,P7}$ is shown in grey, the spectrum calculated by extrapolating with $\gamma_{P5,P7}$ is shown in green, and the spectrum calculated by extrapolating with $\gamma_{P5,P7} - 0.86$ is shown in black. The latter spectrum rolls over smoothly instead of having an unrealistic hardening, and is, as expected, in best agreement with the integral bow-tie analysed channels P9 and P10 (Raukunen et al. 2020), which are shown in red. The spectra of the other major events display similar behaviour, meaning that the method works in producing reasonable estimates of the integral flux above P7.

Appendix D: Annual fluences

The annual integral solar proton fluences F_{10} , F_{30} , F_{60} , F_{100} , and F_{200} and their error estimates $\sigma_{F_{10}}$, $\sigma_{F_{30}}$, $\sigma_{F_{60}}$, $\sigma_{F_{100}}$, and $\sigma_{F_{200}}$ for the years 1984–2019 are presented in Table D.1. The table is also available in a machine-readable format at the CDS.

Table D.1. Annual solar proton fluences and their error estimates for years 1984–2019

Year	F_{10}	$\sigma_{F_{10}}$	F_{30}	$\sigma_{F_{30}}$	F_{60}	$\sigma_{F_{60}}$	F_{100}	$\sigma_{F_{100}}$	F_{200}	$\sigma_{F_{200}}$
1984	$1.05 \cdot 10^9$	$2.53 \cdot 10^7$	$1.80 \cdot 10^8$	$4.85 \cdot 10^6$	$4.30 \cdot 10^7$	$8.19 \cdot 10^5$	$1.39 \cdot 10^7$	$3.08 \cdot 10^5$	$3.42 \cdot 10^6$	$2.45 \cdot 10^5$
1985	$8.31 \cdot 10^7$	$2.79 \cdot 10^6$	$1.22 \cdot 10^7$	$8.81 \cdot 10^5$	$4.23 \cdot 10^6$	$3.49 \cdot 10^5$	$1.86 \cdot 10^6$	$2.66 \cdot 10^5$	$5.92 \cdot 10^5$	$2.53 \cdot 10^5$
1986	$2.69 \cdot 10^8$	$6.77 \cdot 10^6$	$4.88 \cdot 10^7$	$1.19 \cdot 10^6$	$1.33 \cdot 10^7$	$5.71 \cdot 10^5$	$4.57 \cdot 10^6$	$4.00 \cdot 10^5$	$1.17 \cdot 10^6$	$4.00 \cdot 10^5$
1987	$3.01 \cdot 10^7$	$2.14 \cdot 10^6$	$2.35 \cdot 10^6$	$6.82 \cdot 10^5$	$6.96 \cdot 10^5$	$3.54 \cdot 10^5$	$3.54 \cdot 10^5$	$3.12 \cdot 10^5$	$1.50 \cdot 10^5$	$3.27 \cdot 10^5$
1988	$1.44 \cdot 10^8$	$7.71 \cdot 10^6$	$2.77 \cdot 10^7$	$1.73 \cdot 10^6$	$9.97 \cdot 10^6$	$8.14 \cdot 10^5$	$5.15 \cdot 10^6$	$5.10 \cdot 10^5$	$1.98 \cdot 10^6$	$5.03 \cdot 10^5$
1989	$3.23 \cdot 10^{10}$	$8.57 \cdot 10^8$	$8.88 \cdot 10^9$	$1.66 \cdot 10^8$	$2.72 \cdot 10^9$	$4.23 \cdot 10^6$	$9.35 \cdot 10^8$	$1.52 \cdot 10^6$	$2.17 \cdot 10^8$	$9.26 \cdot 10^5$
1990	$1.14 \cdot 10^9$	$3.26 \cdot 10^7$	$2.18 \cdot 10^8$	$6.65 \cdot 10^6$	$8.05 \cdot 10^7$	$1.04 \cdot 10^6$	$3.63 \cdot 10^7$	$4.16 \cdot 10^5$	$1.10 \cdot 10^7$	$3.44 \cdot 10^5$
1991	$1.18 \cdot 10^{10}$	$4.71 \cdot 10^8$	$2.91 \cdot 10^9$	$1.53 \cdot 10^8$	$6.02 \cdot 10^8$	$3.65 \cdot 10^6$	$1.23 \cdot 10^8$	$6.74 \cdot 10^5$	$1.81 \cdot 10^7$	$4.69 \cdot 10^5$
1992	$3.97 \cdot 10^9$	$3.75 \cdot 10^8$	$9.66 \cdot 10^8$	$3.76 \cdot 10^7$	$2.35 \cdot 10^8$	$2.13 \cdot 10^6$	$6.44 \cdot 10^7$	$6.44 \cdot 10^5$	$1.35 \cdot 10^7$	$5.64 \cdot 10^5$
1993	$4.10 \cdot 10^7$	$2.84 \cdot 10^6$	$1.02 \cdot 10^7$	$1.20 \cdot 10^6$	$3.28 \cdot 10^6$	$4.24 \cdot 10^5$	$1.32 \cdot 10^6$	$3.36 \cdot 10^5$	$4.03 \cdot 10^5$	$3.38 \cdot 10^5$
1994	$6.76 \cdot 10^8$	$1.19 \cdot 10^8$	$7.24 \cdot 10^6$	$9.51 \cdot 10^5$	$1.75 \cdot 10^6$	$3.74 \cdot 10^5$	$8.22 \cdot 10^5$	$3.36 \cdot 10^5$	$3.31 \cdot 10^5$	$3.48 \cdot 10^5$
1995	$1.90 \cdot 10^7$	$1.56 \cdot 10^6$	$1.57 \cdot 10^6$	$3.28 \cdot 10^5$	$2.72 \cdot 10^5$	$2.47 \cdot 10^5$	$9.25 \cdot 10^4$	$2.03 \cdot 10^5$	$3.14 \cdot 10^4$	$2.13 \cdot 10^5$
1996	$4.82 \cdot 10^5$	$4.85 \cdot 10^5$	$3.96 \cdot 10^4$	$1.90 \cdot 10^5$	$1.67 \cdot 10^4$	$9.02 \cdot 10^4$	$1.27 \cdot 10^4$	$9.29 \cdot 10^4$	$8.06 \cdot 10^3$	$1.03 \cdot 10^5$
1997	$5.11 \cdot 10^8$	$1.16 \cdot 10^7$	$1.79 \cdot 10^8$	$3.40 \cdot 10^6$	$6.86 \cdot 10^7$	$6.20 \cdot 10^5$	$2.88 \cdot 10^7$	$3.42 \cdot 10^5$	$8.08 \cdot 10^6$	$2.91 \cdot 10^5$
1998	$2.21 \cdot 10^9$	$3.08 \cdot 10^7$	$4.32 \cdot 10^8$	$4.00 \cdot 10^6$	$8.69 \cdot 10^7$	$2.03 \cdot 10^6$	$2.03 \cdot 10^7$	$8.39 \cdot 10^5$	$4.46 \cdot 10^6$	$8.27 \cdot 10^5$
1999	$1.25 \cdot 10^8$	$8.42 \cdot 10^6$	$1.38 \cdot 10^7$	$1.11 \cdot 10^6$	$3.98 \cdot 10^6$	$6.01 \cdot 10^5$	$1.87 \cdot 10^6$	$4.51 \cdot 10^5$	$7.30 \cdot 10^5$	$4.55 \cdot 10^5$
2000	$2.28 \cdot 10^{10}$	$7.94 \cdot 10^7$	$6.84 \cdot 10^9$	$2.59 \cdot 10^7$	$1.72 \cdot 10^9$	$3.29 \cdot 10^6$	$4.10 \cdot 10^8$	$9.55 \cdot 10^5$	$6.24 \cdot 10^7$	$6.41 \cdot 10^5$
2001	$2.61 \cdot 10^{10}$	$1.04 \cdot 10^8$	$5.38 \cdot 10^9$	$1.14 \cdot 10^7$	$1.11 \cdot 10^9$	$4.00 \cdot 10^6$	$2.44 \cdot 10^8$	$8.62 \cdot 10^5$	$3.87 \cdot 10^7$	$5.96 \cdot 10^5$
2002	$3.37 \cdot 10^9$	$3.89 \cdot 10^7$	$6.89 \cdot 10^8$	$6.18 \cdot 10^6$	$1.44 \cdot 10^8$	$1.63 \cdot 10^6$	$3.04 \cdot 10^7$	$5.83 \cdot 10^5$	$4.38 \cdot 10^6$	$5.43 \cdot 10^5$
2003	$1.37 \cdot 10^{10}$	$5.70 \cdot 10^8$	$3.55 \cdot 10^9$	$6.15 \cdot 10^7$	$8.26 \cdot 10^8$	$4.65 \cdot 10^6$	$1.87 \cdot 10^8$	$1.09 \cdot 10^6$	$2.54 \cdot 10^7$	$4.34 \cdot 10^5$
2004	$7.23 \cdot 10^8$	$1.66 \cdot 10^7$	$5.73 \cdot 10^7$	$1.45 \cdot 10^6$	$1.14 \cdot 10^7$	$7.82 \cdot 10^5$	$3.59 \cdot 10^6$	$4.14 \cdot 10^5$	$9.26 \cdot 10^5$	$4.16 \cdot 10^5$
2005	$6.19 \cdot 10^9$	$1.22 \cdot 10^8$	$1.42 \cdot 10^9$	$1.70 \cdot 10^7$	$4.11 \cdot 10^8$	$3.29 \cdot 10^6$	$1.49 \cdot 10^8$	$1.67 \cdot 10^6$	$4.20 \cdot 10^7$	$1.22 \cdot 10^6$
2006	$2.43 \cdot 10^9$	$6.26 \cdot 10^7$	$5.44 \cdot 10^8$	$6.19 \cdot 10^6$	$1.55 \cdot 10^8$	$1.45 \cdot 10^6$	$5.11 \cdot 10^7$	$4.57 \cdot 10^5$	$1.10 \cdot 10^7$	$2.58 \cdot 10^5$
2007	$3.48 \cdot 10^4$	$9.53 \cdot 10^4$	$3.36 \cdot 10^4$	$8.89 \cdot 10^4$	$2.91 \cdot 10^4$	$5.05 \cdot 10^4$	$2.17 \cdot 10^4$	$4.95 \cdot 10^4$	$1.34 \cdot 10^4$	$5.45 \cdot 10^4$
2008	0	0	0	0	0	0	0	0	0	0
2009	0	0	0	0	0	0	0	0	0	0
2010	$6.33 \cdot 10^6$	$2.19 \cdot 10^6$	$8.56 \cdot 10^5$	$4.84 \cdot 10^5$	$2.66 \cdot 10^5$	$2.48 \cdot 10^5$	$1.96 \cdot 10^5$	$2.49 \cdot 10^5$	$1.19 \cdot 10^5$	$2.64 \cdot 10^5$
2011	$3.87 \cdot 10^8$	$1.65 \cdot 10^7$	$5.85 \cdot 10^7$	$2.38 \cdot 10^6$	$1.81 \cdot 10^7$	$1.00 \cdot 10^6$	$7.53 \cdot 10^6$	$8.61 \cdot 10^5$	$2.41 \cdot 10^6$	$8.72 \cdot 10^5$
2012	$8.60 \cdot 10^9$	$2.87 \cdot 10^8$	$1.58 \cdot 10^9$	$1.26 \cdot 10^7$	$3.55 \cdot 10^8$	$3.68 \cdot 10^6$	$9.36 \cdot 10^7$	$9.77 \cdot 10^5$	$1.57 \cdot 10^7$	$7.75 \cdot 10^5$
2013	$1.14 \cdot 10^9$	$9.19 \cdot 10^7$	$1.19 \cdot 10^8$	$1.96 \cdot 10^6$	$2.54 \cdot 10^7$	$9.23 \cdot 10^5$	$7.69 \cdot 10^6$	$6.39 \cdot 10^5$	$1.85 \cdot 10^6$	$6.26 \cdot 10^5$
2014	$1.45 \cdot 10^9$	$3.35 \cdot 10^7$	$2.09 \cdot 10^8$	$3.83 \cdot 10^6$	$4.45 \cdot 10^7$	$1.19 \cdot 10^6$	$1.26 \cdot 10^7$	$6.26 \cdot 10^5$	$3.10 \cdot 10^6$	$6.03 \cdot 10^5$
2015	$2.30 \cdot 10^8$	$2.21 \cdot 10^7$	$1.27 \cdot 10^7$	$1.32 \cdot 10^6$	$4.78 \cdot 10^6$	$7.39 \cdot 10^5$	$2.77 \cdot 10^6$	$7.17 \cdot 10^5$	$1.32 \cdot 10^6$	$7.44 \cdot 10^5$
2016	$7.61 \cdot 10^6$	$1.55 \cdot 10^6$	$8.63 \cdot 10^5$	$5.02 \cdot 10^5$	$2.12 \cdot 10^5$	$3.07 \cdot 10^5$	$1.44 \cdot 10^5$	$3.06 \cdot 10^5$	$7.85 \cdot 10^4$	$3.20 \cdot 10^5$
2017	$2.12 \cdot 10^9$	$6.81 \cdot 10^7$	$5.91 \cdot 10^8$	$7.41 \cdot 10^6$	$1.83 \cdot 10^8$	$1.56 \cdot 10^6$	$6.06 \cdot 10^7$	$7.41 \cdot 10^5$	$1.21 \cdot 10^7$	$5.56 \cdot 10^5$
2018	$3.14 \cdot 10^4$	$1.86 \cdot 10^5$	0	0	0	0	0	0	0	0
2019	0	0	0	0	0	0	0	0	0	0

Notes. All fluence and error values are in units of cm^{-2} .